ARTICLES
PUBLISHED ONLINE: 27 JUNE 2016 | DOI: 10.1038/NNANO.2016.96
nature nanotechnology

Three-dimensional mapping and regulation of action potential propagation in nanoelectronics-innervated tissues

Xiaochuan Dai[1†], Wei Zhou[1†], Teng Gao[1], Jia Liu[1] and Charles M. Lieber[1,2*]

Real-time mapping and manipulation of electrophysiology in three-dimensional (3D) tissues could have important impacts on fundamental scientific and clinical studies, yet realization is hampered by a lack of effective methods. Here we introduce tissue-scaffold-mimicking 3D nanoelectronic arrays consisting of 64 addressable devices with subcellular dimensions and a submillisecond temporal resolution. Real-time extracellular action potential (AP) recordings reveal quantitative maps of AP propagation in 3D cardiac tissues, enable *in situ* tracing of the evolving topology of 3D conducting pathways in developing cardiac tissues and probe the dynamics of AP conduction characteristics in a transient arrhythmia disease model and subsequent tissue self-adaptation. We further demonstrate simultaneous multisite stimulation and mapping to actively manipulate the frequency and direction of AP propagation. These results establish new methodologies for 3D spatiotemporal tissue recording and control, and demonstrate the potential to impact regenerative medicine, pharmacology and electronic therapeutics.

Developments in cardiac tissue engineering over the past two decades[1–5] have substantially advanced *in vitro* models for drug screening[6–8] and disease studies[9], as well as *in vivo* implants to replace diseased or damaged tissues[10,11] such as those resulting from myocardial infarction[11]. However, effective methodologies for the real-time 3D mapping and manipulation of electrical activity in studies of tissue development, drug modulation and implantation have thus far been missing. Optical imaging using exogenous or genetically encoded voltage-sensitive dyes[12–14] has allowed high spatial-resolution mapping of AP propagation but can be limited by a relatively low temporal resolution in 3D scanning[13–15] and light scattering in tissues[13,15]. On the other hand, multiplexed electrical recordings with planar microelectrodes[8,16] or field-effect transistor (FET)[17,18] arrays can map APs with a submillisecond temporal resolution, but have been limited to studies of 2D cultured cells[17] or the surfaces of 3D tissue samples[18].

To overcome the key gaps in existing optical voltage sensing and planar electrode device methods, we previously introduced a 3D nanoelectronics scaffold concept that could access the cellular response from within engineered tissues[19], although the size and mechanical mismatches precluded 3D tissue mapping. Here we present a new class of nanoelectronics that mimic tissue scaffolds, designed with both dimensions and mechanical properties comparable to the conventional cardiac tissue scaffold poly(lactic-co-glycolic acid) (PLGA) electro-spun fibers[2,4,20] (Supplementary Information). These new nanoelectronics have been used as cardiac tissue scaffolds alone or together with PLGA auxiliary layers to enable real-time mapping of APs across 3D samples with submillisecond temporal resolution. In addition, the incorporation of stimulator electrodes allows for simultaneous active control and mapping of cardiac tissue electrophysiology in three dimensions.

3D activity mapping from nanoelectronics–cardiac tissues

The 3D nanoelectronics–cardiac tissues were prepared using a strategy that involves three major steps (Fig. 1a–c). First, 350–750-nm-thick 2D polymeric meshes with embedded nanoelectronics are fabricated on a substrate by photolithography on an Ni release layer with free-standing structures left by Ni etching. To meet the feature size and mechanical property criteria for tissue-scaffold-like nanoelectronics, we used a high-density silicon nanowire assembly to obtain a >95% yield of free-standing FET arrays with a 1–2 μm footprint (Supplementary Information, Fig. 1a and Supplementary Fig. 4a). Importantly, this new design has stiffness values of 2.8×10^{-16} N m^{-2} and 2.9×10^{-17} N m^{-2} for the SU-8/metal/SU-8 and SU-8 elements, respectively, comparable to 1 μm diameter PLGA electro-spun fibers (with a stiffness value of 1.0×10^{-16} N m^2) used as cardiac tissue scaffolds[2,4,20] (Supplementary Information); that is, the free-standing nanoelectronics are similar to tissue scaffolds in terms of mechanical properties.

The 2D free-standing meshes were folded into 3D nanoelectronic scaffolds (Fig. 1b; Supplementary Fig. 4b–f) and neonatal rat ventricular cells were then seeded and cultured to yield nanoelectronics–cardiac tissue (Fig. 1c; Supplementary Information). Although these studies focus on almost planar structures as are typical for engineered cardiac patches[3,7,19], nanoelectronic scaffolds could also be folded over curved structures to yield non-planar structures or even rolled into cylinders. Representative confocal microscopy images taken at 7 days *in vitro* (DIV; Supplementary Fig. 6) show characteristic adult sarcomere lengths of 2.1 ± 0.1 μm (ref. 21) aligned to the scaffold. Extracellular cardiac AP signals recorded from 4 × 4 FET sensors in a single layer across a 5 × 5 mm^2 domain (Fig. 1d) show a synchronized beating rate of 1.8 Hz, an amplitude of 1–2 mV and a peak width of ~1 ms from all 16 channels, consistent with extracellular recording results of FET devices on planar chips[17]. Higher-resolution examination of these peaks (Fig. 1e) reveals a submillisecond

[1]Department of Chemistry and Chemical Biology, Harvard University, Cambridge, Massachusetts 02138, USA. [2]Harvard John A. Paulson School of Engineering and Applied Sciences, Harvard University, Cambridge, Massachusetts 02138, USA. †These authors contributed equally to this work.
*e-mail: cml@cmliris.harvard.edu

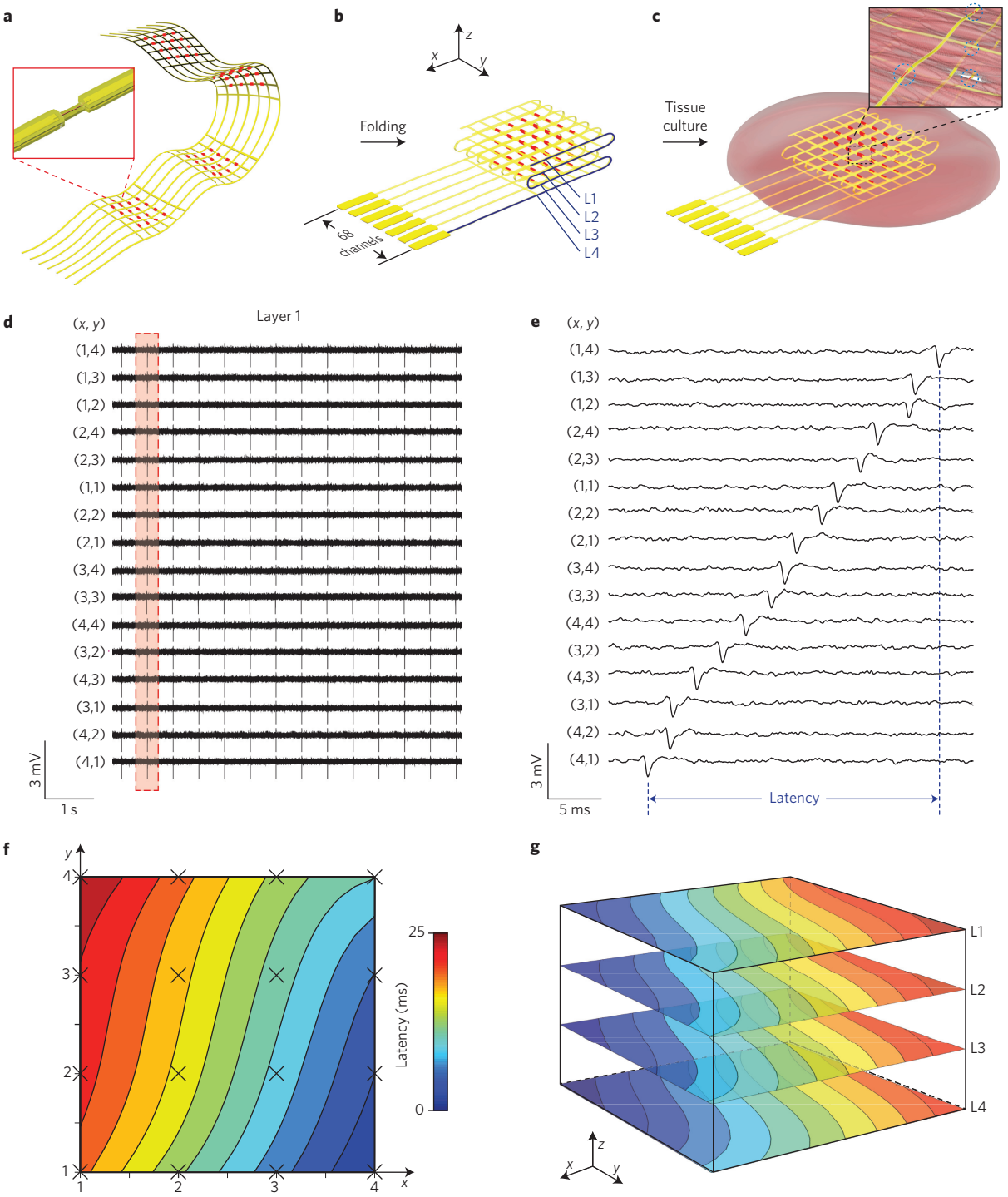

Figure 1 | 3D spatiotemporal mapping of APs. a, Schematic of the free-standing macroporous nanoelectronic scaffold with nanowire FET arrays (red dots). Inset, one nanowire FET. In **a**–**c**, a limited number of input/output leads are shown for clarity; the total number for the design as indicated in **b** is 68. **b**, Folded 3D free-standing scaffolds with four layers of individually addressable FET sensors. **c**, Schematic of nanoelectronic scaffold/cardiac tissue resulting from the culturing of cardiac cells within the 3D folded scaffold. Inset, the nanoelectronic sensors (blue circles) innervate the 3D cell network. **d**, Simultaneous traces recorded from 16 sensors in the top layer (L1) of the nanoelectronics–cardiac tissue. The (x,y) coordinates of each element from the 4 × 4 array are shown. See Supplementary Data for the original data. **e**, Zoom-in of a single AP spike recorded from each device during the time indicated by the dashed red box in **d**. The time latency between the APs recorded from different devices is evident and specifically indicated for FETs (4,1) to (1,4). **f**, Isochronal map of time latency in L1; the mapping area is ~25 mm^2. **g**, 3D isochronal map of time latency through the sample, where L1–L4 correspond to the four layers of 4 × 4 device arrays innervating the cardiac tissue. The mapping area is ~25 mm × 25 mm × 200 μm.

time latency between any given set of AP peaks recorded by the 16 FET sensors, where the intrinsic temporal resolution of the device is 0.01–0.05 ms (Supplementary Information)—substantially better than the timescale of the observed AP peak or peak latency.

To better visualize the AP propagation, we plot these data from the single layer as an isochronal map of time latency (Fig. 1f). This map, which covers a 5 × 5 mm^2 area of tissue, shows that the AP wavefront propagates from the FET(x,y = 4,1) to FET(1,4).

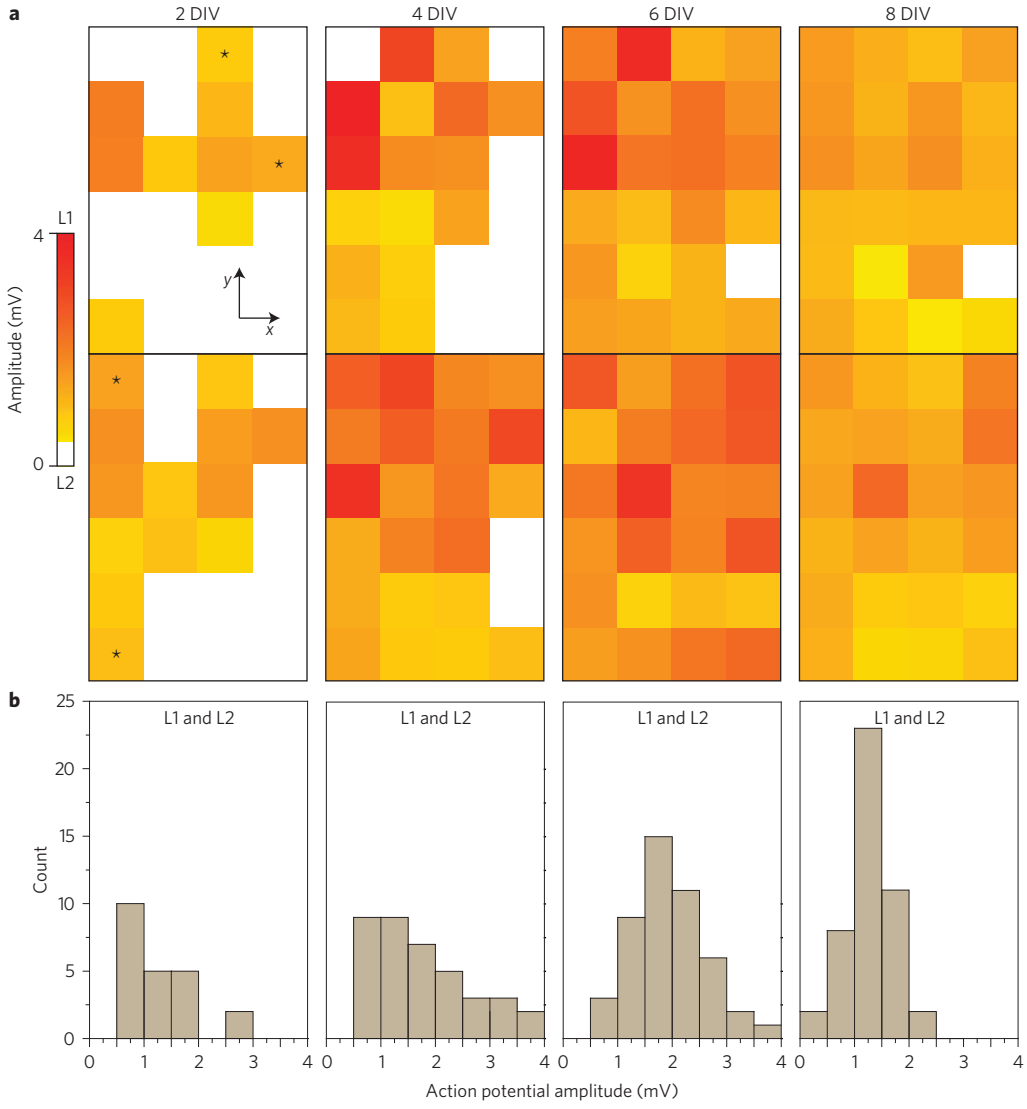

Figure 2 | AP evolution during tissue development. a, Amplitudes of spontaneous extracellular APs recorded from the 4 × 6 nanowire FET arrays in two layers at 2, 4, 6 and 8 DIV. White squares correspond to coordinates where extracellular APs are absent or below the detection limit (1 standard deviation of the noise level). Time-dependent data recorded from four devices (2 × L1 and 2 × L2) indicated with asterisks at 2 DIV are shown in Supplementary Fig. 5. **b**, Histogram of extracellular AP amplitudes recorded from the 3D nanoelectronics–cardiac tissue sample at 2, 4, 6 and 8 DIV.

Combining the spatiotemporal AP recording results from all the 64 FET sensors designed in four layers, we plot a 3D isochronal map of time latency (Fig. 1g) that visualizes the 3D waveform of AP conduction in the nanoelectronics–cardiac tissue. The similar but not identical latency between z coordinates is consistent with the small (50 μm) distance between neighbouring nanoelectronic mesh layers and also highlights the well-developed 3D coherence of the cellular networks. The average conduction velocity (28 ± 2 cm s^{-1}) is very similar to that of *in vivo* neonatal rat heart tissue (21–27 cm s^{-1}) (ref. 5), thus supporting the 3D coherence.

3D activity mapping during cardiac tissue development

We have investigated the evolution of electrophysiological activity during culture and tissue development using nanoelectronics–cardiac tissues. 3D real-time mapping of APs carried out at 2, 4, 6 and 8 DIV using a $6 \times 4 \times 2$ array of integrated FETs (Fig. 2a) highlights several key points. Qualitatively, analyses of recorded AP maps show that the spontaneous beating volume expands to the entire sample for ≥6 DIV. Quantitative analyses of these data show that the percentage volume of detectable activity at 2, 4, 6 and 8 DIV are ~46, 79, 98 and 98%, respectively. Third, examination of real-time AP data recorded at 2 DIV where the regions of spontaneous beating tissue are sparse (Supplementary Fig. 8) demonstrates that beating is synchronized within and between different device layers. These latter results suggest that the 3D topology of the conducting pathways develops early during the maturation of engineered cardiac tissue. More generally, although progress has been made on the 3D structural visualization of cardiac tissue development[22], it is still difficult to directly map the 3D functional networking during tissue maturation—thus the nanoelectronics–cardiac tissue provides a complementary method to address this key issue.

In addition, analysis of the AP data further demonstrates that at 2, 4, 6 and 8 DIV the beating rates (Supplementary Fig. 9) are 346, 470, 52 and 38 beats per minute, respectively. The beating rate shows a substantial decrease after 4 DIV, as expected during the maturation of rat cardiac tissue[23,24]. The averaged extracellular AP amplitudes from the samples at 2, 4, 6 and 8 DIV (Fig. 2b)—$1.27 \pm 42\%$, $1.77 \pm 49\%$, $1.92 \pm 34\%$ and $1.27 \pm 32\%$ mV, respectively—also exhibit averaged amplitude variations, although the values are

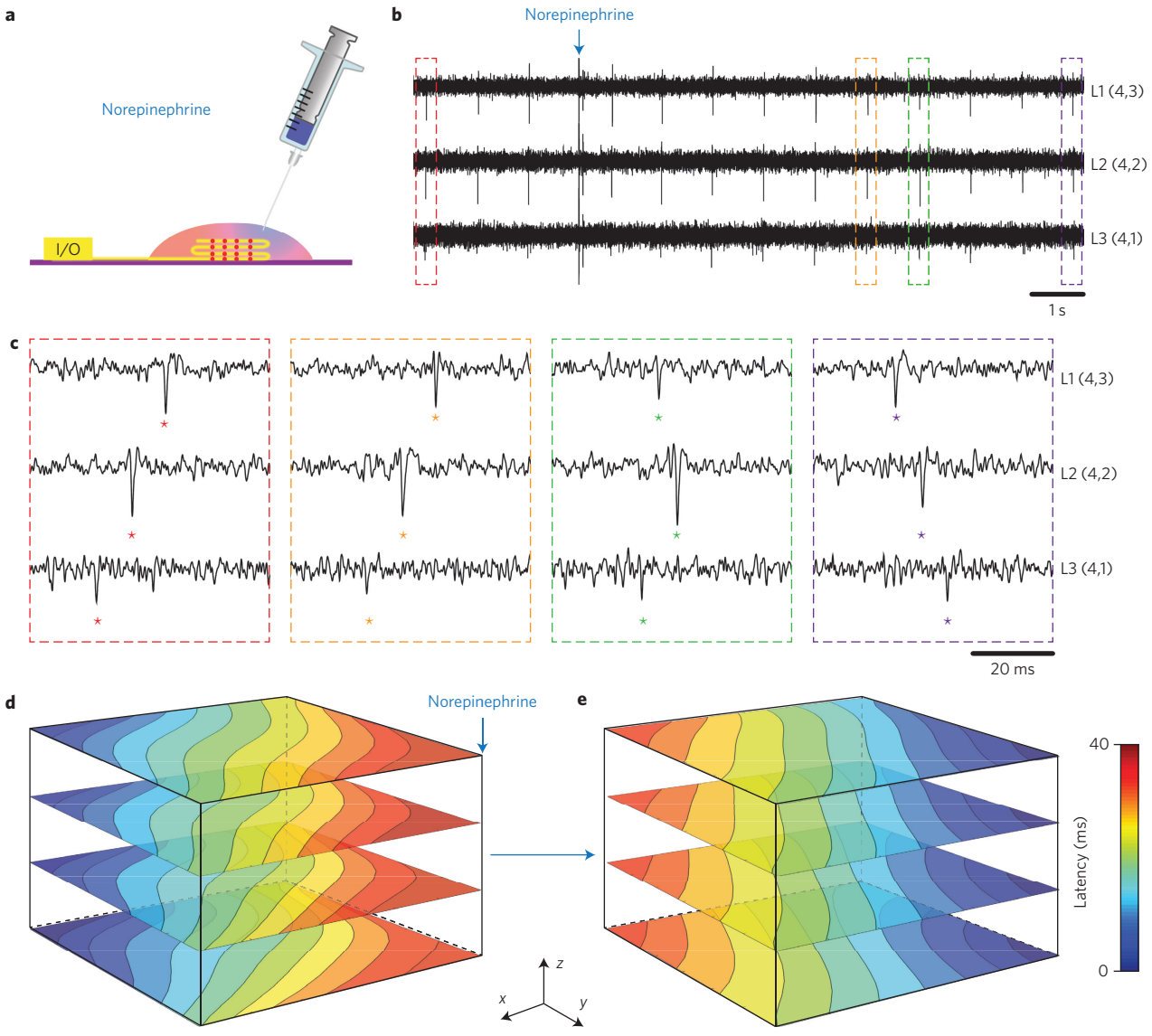

Figure 3 | Arrhythmia induced by localized norepinephrine injection. a, Schematic of the measurement set-up highlighting the syringe injection of norepinephrine at a localized spot on the 3D nanoelectronics–cardiac tissue. **b**, Time-dependent traces from three sensors in L1, L2 and L3 with synchronized and periodic APs. The blue arrow indicates the injection of ~25 μl norepinephrine at a concentration of 100 μM. **c**, Zoom-in of the four coloured box regions in **b**, depicting the time latency between the APs before and 5–10 s after the addition of norepinephrine. **d**,**e**, 3D isochronal time latency maps before (**d**) and 5 min after (**e**) local norepinephrine injection. The blue arrow in **d** indicates the injection position.

statistically overlapping. We do note that the smallest coefficient of variation (±32%) occurs at 8 DIV, suggesting an increase in the uniformity of the amplitudes and cell growth on the scaffolds along with tissue development, as the extracellular AP amplitudes are affected by factors such as the cell-to-device distance and sealing[25]. These results show that nanoelectronics–cardiac tissue can provide insight into the electrophysiological development in 3D, and thus could impact research in cardiac tissue engineering and regeneration, including stem cell differentiation, growth factors and ischemia[26,27].

3D monitoring of cardiac pharmacological and disease models

We have used nanoelectronics–cardiac tissue to investigate responses to drugs (Fig. 3; Supplementary Figs 10 and 11; Supplementary Information) with a focus on the 3D dynamics of AP propagation in a drug-induced ventricular arrhythmia model[28]. β-Adrenergic receptor agonists such as norepinephrine are used to treat heart failure, but can produce ventricular arrhythmia and sudden cardiac death during local injection[28]. We investigate this phenomenon by focal injection of norepinephrine on 3D nanoelectronics–cardiac tissues (Fig. 3a) while simultaneously recording real-time 3D APs. Representative data from three FET sensors in different layers before and after norepinephrine injection near sensor L1(4,3) (Fig. 3b–c) highlight the dynamic instability of the conduction pathway. The examination of time-correlated AP peaks from these three devices before and 5–10 s post-injection (Fig. 3c) shows that the AP propagates initially from sensor L3(4,1) to L1(4,3), but that ~10 s after drug injection the propagation direction is reversed. In the intermediate regime, the recorded peaks indicate an earlier depolarization around sensor L1(4,3), which then leads to the reversal of the overall propagation direction. At a steady-state post-injection, the full 3D AP isochronal maps (Fig. 3d) clearly show that a new stable 3D AP propagation direction arising from the norepinephrine injection location has overridden the original pacemaker foci.

In contrast, independent experiments with homogeneous perfusion of norepinephrine (Supplementary Fig. 10) and 1-heptanol

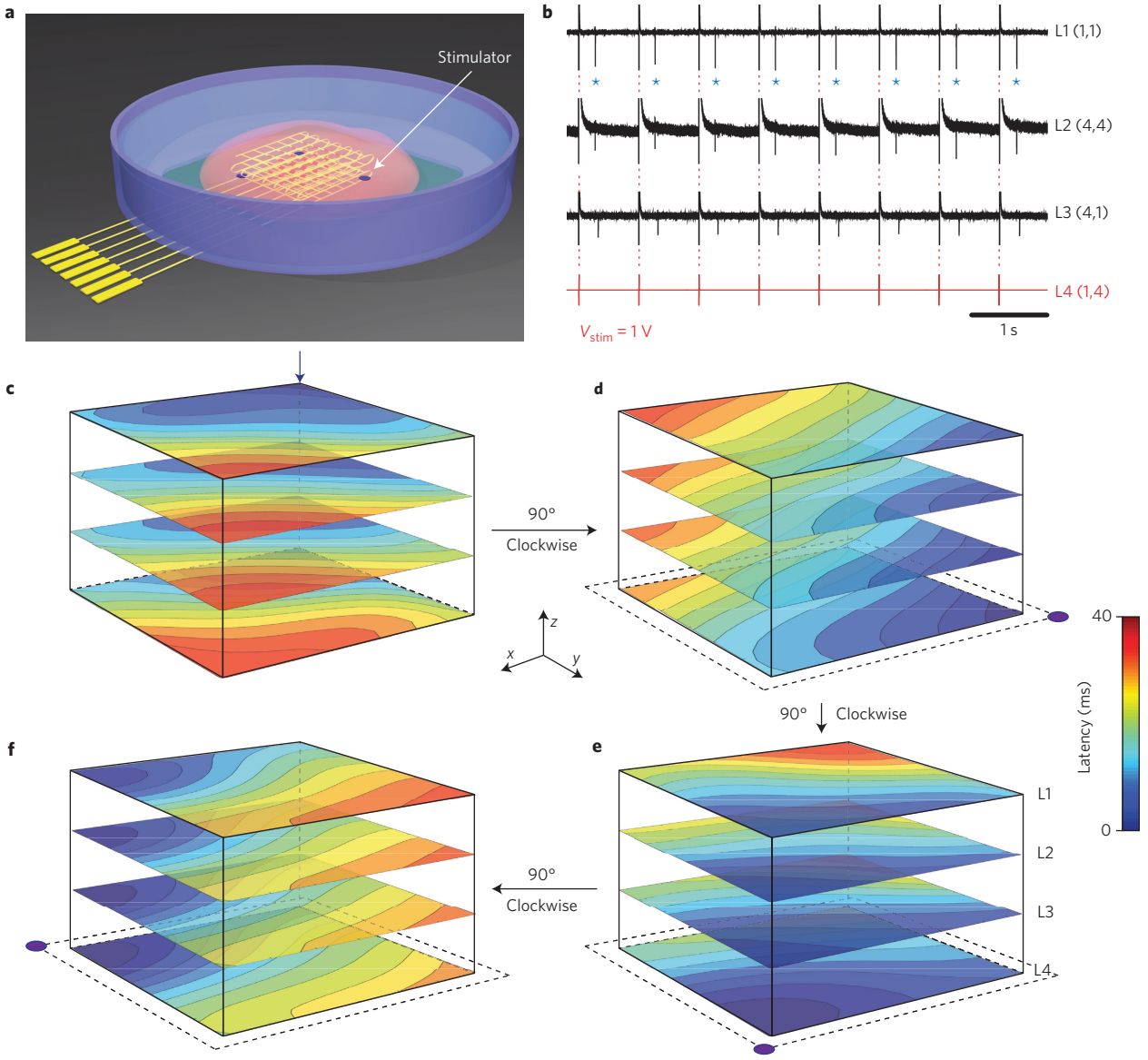

Figure 4 | Active spatiotemporal regulation of APs. a, Schematic illustrating the positions of the individually addressable stimulator electrodes (purple dots) in the nanoelectronic scaffold. **b**, Time-dependent traces recorded from nanowire FETs in layers L1, L2 and L3 under a periodic biphasic stimulation spike train in L4. The stimulation peak width, amplitude (V_{stim}) and frequency were 1 ms, 1 V and 1.25 Hz, respectively. Blue asterisks in the L1 trace highlight APs (downward spikes) versus capacitive coupling peaks (red dashed lines). **c**–**f**, 3D isochronal time latency maps for the original pacemaker foci location (**c**, blue arrow), and sequential 90° clockwise rotations (**d**–**f**) of the AP propagation direction using the indicated simulator electrodes (lower corners in **d** to **f**).

(Supplementary Fig. 11) serve both as controls and highlight extra capabilities of the nanoelectronics–cardiac tissue for pharmacological assays. Homogeneous norepinephrine perfusion yields a 150% increase in the steady-state beating rate and, importantly, measurements (Supplementary Fig. 10b) demonstrated full 3D synchronization of the APs from sensors in different regions of the tissue, in contrast to focal injection (Fig. 3). Interestingly, the high-temporal-resolution 3D mapping exhibited a transient conduction velocity increase over the initial 60 s of perfusion (a 17% peak increase ~30 s after the start). Perfusion of the gap junction blocker[8] 1-heptanol, which inhibits cell-to-cell current conduction via intercellular gap junctions, results in a uniform decrease in the AP conduction velocity/increase in latency (Supplementary Fig. 11b–c). High-temporal-resolution characterization of the AP conduction velocity at the single peak level without averaging allows the diffusion and action of 1-heptanol to be monitored from the top surface through the interior of the tissue in real time. These temporally and spatially varying effects, including the dynamic instability associated with non-uniform norepinephrine addition (Fig. 3), would otherwise have been difficult to detect using methods that require averaging of the AP peaks and/or scanning to resolve accurate time latency in 3D.

Simultaneous mapping and manipulation of cardiac activity

Beyond real-time mapping of propagating APs, the incorporation of stimulators could open up the possibility of simultaneous manipulation of the tissue electrophysiology as required for closed-loop control of cardiac activity and/or to treat abnormalities. To this end, we incorporated individually addressable electrical stimulators together with nanowire FET sensors into the nanoelectronic scaffolds (Fig. 4a; Supplementary Information). As an illustration, the application of a variable amplitude 1.25 Hz stimulation spike train to one of the stimulators in the nanoelectronics–cardiac tissue (Fig. 4b and Supplementary Fig. 12) yields AP peaks recorded

in different regions (L1–L3) of the tissue locked to the stimulation frequency when the stimulator pulse amplitude is 1 V; and for amplitudes ≤100 mV the natural ~1 Hz beating frequency of the tissue is observed (Supplementary Fig. 12). Interestingly, the coefficient of variation of the beating rate increases by 4.3× (from 2.7 to 11.7%) as the stimulation amplitude increases from 1 to 100 mV (Supplementary Fig. 12f), suggesting a dynamic instability of cardiomyocytes before the locking to the pacing rate. Further studies of stimulation at 1 V versus frequency (Supplementary Fig. 13) show stable locking of the tissue beating for 1.25, 1.67 and 2.5 Hz stimulation, and thus suggest the potential to modulate cardiac activity on demand.

Last, we use the active stimulation and monitoring capabilities to illustrate spatial manipulation of the AP propagation direction within tissues. Specifically, a nanoelectronics–cardiac tissue sample with the original pacemaker foci located at L1(1,1) (Fig. 4c) was sequentially paced by stimulator electrodes located at L4(1,4), L4(4,4) and L4(4,1). Following stimulation to lock the AP pacemaker foci to a given stimulator position, the recorded 3D APs plotted as latency maps (Fig. 4d–f) demonstrate clearly that the AP propagation directions are rotated sequentially 90° at each step. These results provide a proof-of-concept for spatiotemporal manipulation together with real-time 3D interrogation of propagating APs, and thus offer the potential for sophisticated modulation of cardiac tissue electrophysiology compared with conventional stimulators[29].

The results presented here open up high-temporal-resolution 3D electrophysiology mapping and manipulation in engineered cardiac tissues, and have the potential to affect several areas of cardiac research including *in vitro* models for drug-screening[6–8] and *in vivo* implants to replace diseased or damaged tissues[10,11]. In this latter context, we envision our nanoelectronics–cardiac tissue could be surgically implanted with the input/output wiring (from the scaffold) allowing for continuous monitoring and stimulation of the implants. Alternatively, it might be interesting to consider syringe co-injection of both nanoelectronic scaffolds[30] and cardiac progenitor cells or stem cells[31] directly into damaged tissues for 'smart' repairs with integrated self-monitoring and self-regulation functionality.

More generally, the successful miniaturization of the nanoelectronic scaffolds, which allows the size and mechanical properties to be matched to conventional passive tissues scaffolds, and the incorporation of large numbers of addressable nanoelectronic devices, which allows 3D mapping, can enable facile integration in a range of engineered tissues for drug screening models through regenerative medicine[32]. For example, using softer nanoelectronic and auxiliary scaffolds we could extend the application to engineered 3D neuronal tissues[19]. Rolling the tissue-scaffold-mimicking nanoelectronics into tubular structures could also allow blood vessels to be engineered[19] and the separation of distinct cell layers with nanolectronic scaffold layers could be used to study blood brain barrier[33,34] tissue models in unique ways. Finally, we believe it will be important to extend the functionality of the nanoelectronic scaffolds by integrating chemical sensors[35], pressure sensors[36,37], light-emitting-devices[38] and active matrix addressing[39] as these could substantially expand the capabilities for monitoring and stimulation.

Methods

Methods and any associated references are available in the online version of the paper.

Received 21 January 2016; accepted 10 May 2016;
published 27 June 2016; corrected online 21 July 2016

References

1. Langer, R. & Vacanti, J. P. Tissue engineering. *Science* **260,** 920–926 (1993).
2. Eschenhagen, T. & Zimmermann, W. H. Engineering myocardial tissue. *Circ. Res.* **97,** 1220–1231 (2005).
3. Shimizu, T. *et al.* Fabrication of pulsatile cardiac tissue grafts using a novel 3-dimensional cell sheet manipulation technique and temperature-responsive cell culture surfaces. *Circ. Res.* **90,** e40 (2002).
4. Dvir, T., Timko, B. P., Kohane, D. S. & Langer, R. Nanotechnological strategies for engineering complex tissues. *Nature Nanotech.* **6,** 13–22 (2011).
5. Papadaki, M. *et al.* Tissue engineering of functional cardiac muscle: molecular, structural, and electrophysiological studies. *Am. J. Physiol. Heart Circ. Physiol.* **280,** 168–178 (2001).
6. Hansen, A. *et al.* Development of a drug screening platform based on engineered heart tissue. *Circ. Res.* **107,** 35–44 (2010).
7. Grosberg, A., Alford, P. W., McCain, M. L. & Parker, K. K. Ensembles of engineered cardiac tissues for physiological and pharmacological study: heart on a chip. *Lab Chip* **11,** 4165–4173 (2011).
8. Natarajan, A. *et al.* Patterned cardiomyocytes on microelectrode arrays as a functional, high information content drug screening platform. *Biomaterials* **32,** 4267–4274 (2011).
9. Griffith, L. G. & Naughton, G. Tissue engineering-current challenges and expanding opportunities. *Science* **295,** 1009–1014 (2002).
10. Furuta, A. *et al.* Pulsatile cardiac tissue grafts using a novel three-dimensional cell sheet manipulation technique functionally integrates with the host heart, *in vivo*. *Circ. Res.* **98,** 705–712 (2006).
11. Zimmermann, W. H. *et al.* Engineered heart tissue grafts improve systolic and diastolic function in infarcted rat hearts. *Nature Med.* **12,** 452–458 (2006).
12. St-Pierre, F. *et al.* High-fidelity optical reporting of neuronal electrical activity with an ultrafast fluorescent voltage sensor. *Nature Neurosci.* **17,** 884–889 (2014).
13. Herron, T. J., Lee, P. & Jalife, J. Optical imaging of voltage and calcium in cardiac cells & tissues. *Circ. Res.* **110,** 609–623 (2012).
14. Kralj, J. M., Douglass, A. D., Hochbaum, D. R., Maclaurin, D. & Cohen, A. E. Optical recording of action potentials in mammalian neurons using a microbial rhodopsin. *Nat. Methods* **9,** 90–95 (2012).
15. Huisken, J., Swoger, J., Del Bene, F., Wittbrodt, J. & Stelzer, E. H. K. Optical sectioning deep inside live embryos by selective plane illumination microscopy. *Science* **305,** 1007–1009 (2004).
16. Kim, D. H. *et al.* Materials for multifunctional balloon catheters with capabilities in cardiac electrophysiological mapping and ablation therapy. *Nature Mater.* **10,** 316–323 (2011).
17. Cohen-Karni, T., Timko, B. P., Weiss, L. E. & Lieber, C. M. Flexible electrical recording from cells using nanowire transistor arrays. *Proc. Natl Acad. Sci. USA* **106,** 7309–7313 (2009).
18. Viventi, J. *et al.* A conformal, bio-interfaced class of silicon electronics for mapping cardiac electrophysiology. *Sci. Transl. Med.* **2,** 24ra22 (2010).
19. Tian, B. Z. *et al.* Macroporous nanowire nanoelectronic scaffolds for synthetic tissues. *Nature Mater.* **11,** 986–994 (2012).
20. Place, E. S., George, J. H., Williams, C. K. & Stevens, M. M. Synthetic polymer scaffolds for tissue engineering. *Chem. Soc. Rev.* **38,** 1139–1151 (2009).
21. Zhang, D. *et al.* Tissue-engineered cardiac patch for advanced functional maturation of human ESC-derived cardiomyocytes. *Biomaterials* **34,** 5813–5820 (2013).
22. Yelbuz, T. M., Choma, M. A., Thrane, L., Kirby, M. L. & Izatt, J. A. Optical coherence tomography – a new high-resolution imaging technology to study cardiac development in chick embryos. *Circulation* **106,** 2771–2774 (2002).
23. Miragoli, M., Gaudesius, G. & Rohr, S. Electrotonic modulation of cardiac impulse conduction by myofibroblasts. *Circ. Res.* **98,** 801–810 (2006).
24. Khademhosseini, A. *et al.* Microfluidic patterning for fabrication of contractile cardiac organoids. *Biomed. Microdev.* **9,** 149–157 (2007).
25. Timko, B. P., Cohen-Karni, T., Qing, Q., Tian, B. & Lieber, C. M. Design and implementation of functional nanoelectronic interfaces with biomolecules, cells, and tissue using nanowire device arrays. *IEEE Trans. Nanotechnol.* **9,** 269–280 (2010).
26. Zhang, J. H. *et al.* Functional cardiomyocytes derived from human induced pluripotent stem cells. *Circ. Res.* **104,** e30 (2009).
27. Laflamme, M. A. *et al.* Cardiomyocytes derived from human embryonic stem cells in pro-survival factors enhance function of infarcted rat hearts. *Nature Biotechnol.* **25,** 1015–1024 (2007).
28. Myles, R. C., Wang, L. G., Kang, C. Y., Bers, D. M. & Ripplinger, C. M. Local beta-adrenergic stimulation overcomes source-sink mismatch to generate focal arrhythmia. *Circ. Res.* **110,** 1454–1464 (2012).
29. Iravanian, S. *et al.* Functional reentry in cultured monolayers of neonatal rat cardiac cells. *Am. J. Physiol. Heart Circ. Physiol.* **285,** 449–456 (2003).
30. Liu, J. *et al.* Syringe-injectable electronics. *Nature Nanotech.* **10,** 629–636 (2015).
31. Garbern, J. C. & Lee, R. T. Cardiac stem cell therapy and the promise of heart regeneration. *Cell Stem Cell* **12,** 689–698 (2013).
32. Wobma, H. & Vunjak-Novakovic, G. Tissue engineering and regenerative medicine 2015: a year in review. *Tissue Eng. Part B Rev.* **22,** 101–113 (2016).
33. Wong, A. D. *et al.* The blood-brain barrier: an engineering perspective. *Front. Neuroeng.* **6,** 7 (2013).
34. Wang, X. Y. *et al.* Engineering interconnected 3D vascular networks in hydrogels using molded sodium alginate lattice as the sacrificial template. *Lab Chip* **14,** 2709–2716 (2014).

35. McAlpine, M. C., Ahmad, H., Wang, D. W. & Heath, J. R. Highly ordered nanowire arrays on plastic substrates for ultrasensitive flexible chemical sensors. *Nature Mater.* **6,** 379–384 (2007).
36. Annabi, N. *et al.* Hydrogel-coated microfluidic channels for cardiomyocyte culture. *Lab Chip* **13,** 3569–3577 (2013).
37. Wang, C. *et al.* User-interactive electronic skin for instantaneous pressure visualization. *Nature Mater.* **12,** 899–904 (2013).
38. Huang, Y., Duan, X. & Lieber, C. M. Nanowires for integrated multicolor nanophotonics. *Small* **1,** 142–147 (2005).
39. Takei, K. *et al.* Nanowire active-matrix circuitry for low-voltage macroscale artificial skin. *Nature Mater.* **9,** 821–826 (2010).

Acknowledgements

The authors thank R. Liao and D. Zhang for the inspiring discussion on cardiac electrophysiology and tissue engineering. The authors thank J. L. Huang for the assistance on instrumentation. This work was supported by National Institutes of Health Director's Pioneer and National Security Science and Engineering Faculty Fellow awards (to C.M.L.).

Author contributions

X.D., W.Z. and C.M.L. conceived and designed the experiments. X.D., W.Z., T.G. and J.L. performed the experiments and analysed the data. X.D., W.Z. and C.M.L. co-wrote the paper. All authors discussed the results and commented on the manuscript.

Additional information

Supplementary information is available in the online version of the paper. Reprints and permissions information is available online at www.nature.com/reprints. Correspondence and requests for materials should be addressed to C.M.L.

Competing financial interests

The authors declare no competing financial interests.

Methods

Nanowire synthesis. The Si nanowires (with an average length of 30 μm) were synthesized on a SiO_2/Si substrate (p type Si, 0.005 Ω cm^{-1}, 600 nm oxide, Nova Electronic Materials, LLC.) by a gold nanoparticle-catalysed vapour–liquid–solid growth method.

Fabrication of free-standing nanoelectronic mesh scaffolds. The 2D free-standing macroporous nanoelectronic mesh scaffolds were fabricated on the oxide surface of the SiO_2/Si substrates before being released from the substrate. Key steps used in the fabrication were as follows. (1) a 100 nm-thick nickel relief film was deposited on the substrate by thermal evaporation using photolithography (PL). (2) A 350 nm-thick layer of SU-8 photoresist (2000.5; MicroChem Corporation) was spin coated over the entire substrate, followed by ultraviolet exposure to define an array of rectangular pads. (3) The Si nanowires were transferred onto the target Si wafer with a selectively patterned SU-8 layer using a lubricant-assisted contact printing method. Nanowires arrays were selectively transferred onto the pre-defined SU-8 pad arrays. (4) PL was used to pattern the mesh-like bottom SU-8 layer, connecting the pre-defined SU-8 pad arrays with nanowires that serve as a passivating and supporting layer. (5) PL was used to pattern symmetrical Cr/Pd/Cr (1.5/50/1.5 nm) metal source/drain contacts followed by thermal evaporation and a sequential lift-off process, forming Si nanowire FET sensor arrays on SU-8 meshes. (6) Another top SU-8 passivation layer was patterned using PL. In addition, four circular palladium/platinum electrodes (50/50 nm) were integrated into the nanoelectronic mesh scaffolds as electrical stimulators at four corners in the layer 4 (Fig. 4a). (For more details see Supplementary Methods)

Folding nanoelectronic mesh structures into 3D scaffolds. Free-standing nanoelectronic meshes with Si nanowire FETs were released from the Si wafer by etching the 100 nm nickel relief layer (Nickel Etchant TFB, Transene Company, Inc.). The nanoelectronic mesh was rinsed with deionized water and stored in deionized water. The free-standing nanoelectronic mesh scaffolds were folded into a multilayer structure, with the alignment assisted by optical microscope. To control a larger separation distance between the different mesh layers, a 50 μm thick PLGA electrospun fibre film was placed between each mesh layer during the folding step. The aligned and folded mesh scaffolds were fixed by Kwik-Sil silicone adhesive (World Precision Instruments, Inc.) at the boundaries after each folding step. (For more details see Supplementary Methods)

Synthetic nanoelectronics-innervated cardiac tissues. Before cell plating, the nanoelectronic mesh scaffolds were thoroughly immersed in a 0.5% fibronectin (F1141, Sigma-Aldrich Corporation)/0.02% gelatin (Fisher Scientific) solution for 2 h for surface modification. Primary neonatal rat cardiomyocytes were prepared according to previously published procedures[17,19]. In brief, intact ventricles were isolated from 1–3 day-old Sprague/Dawley rats and were then digested at 37 °C in Hanks' balanced salt solution containing collagenase (class II, Worthington Biochemical Corporation). Isolated cells were purified through pre-plating in a flask for 2 h to reduce the percentage of non-cardiomyocyte cells. The collected cells were then concentrated and plated at a cell density of $3–6 \times 10^6$ cm^{-2}. (For more details see Supplementary Methods).

Electrophysiology measurements. All of the electrophysiology measurements were carried out at 37 °C (TC-344D temperature controller, Warner Instruments Corporation) and in a Tyrode solution (Sigma-Aldrich Corporation). The conductance of the Si nanowire FETs was measured with a d.c. bias set to 100 mV. The drain current was amplified with 16-channel preamplifier (SIM918 Precision current preamplifier, Stanford Research System) and the output data were bandpass filtered (0–6,000 Hz, home-made system) and recorded at an acquisition rate of 20–100 kHz using a 16-channel A/D converter (Digidata 1440A; Molecular Devices) interfaced with a computer running the pClamp electrophysiology software (version 10.2, Molecular Devices, Axon Laboratory). Data analysis was carried out using OriginPro (version 8.1, Origin Lab Corp.) and Matlab (version R2011a, Mathworks).

Corrigendum: Three-dimensional mapping and regulation of action potential propagation in nanoelectronics-innervated tissues

Xiaochuan Dai, Wei Zhou, Teng Gao, Jia Liu and Charles M. Lieber

Nature Nanotechnology http://dx.doi.org/10.1038/nnano.2016.96 (2016); published online 27 June 2016; corrected online 21 July 2016.

In the version of this Article originally published online, in Fig. 1e, the traces for devices (1,2) and (2,3) were incorrect. This has now been corrected in all versions of the Article. In addition, the original data for Fig. 1d (from which Fig. 1e was extracted) is now provided as Supplementary Data.